Chemical Science

Check for updates

All publication charges for this article have been paid for by the Royal Society of Chemistry

BaSbBS₄: a record-high-performance birefringent crystal identified by a target-driven closed-loop strategy†

Ming-Zhi Zhang, [ab] Yue Zhao, [a] Chun-Li Hu [*a] and Jiang-Gao Mao [ID] [*ab]

Exploring infrared (IR) birefringent materials with both large birefringence (Δn) and wide band gaps (E_g) is urgently demanded for high-power optoelectronic applications and has long been a tough challenge due to the intrinsic contradictory relationship between the two metrics. Herein, we developed a target-driven closed-loop framework in coupling with functional motif and crystal structure screening, deep learning assisted high-throughput optical property computation, targeted experiment and mechanism investigation, enabling efficient discovery of potential birefringent materials. Utilizing it, a batch of superior IR birefringent crystals containing planar $[BS_3]^{3-}$ and/or stereochemically active lone pair (SCALP) groups ($[SbS_3]^{3-}$, $[SnS_3]^{4-}$, *etc.*) were identified: six with huge birefringence ($\Delta n > 1.0$) and three with both large birefringence ($\Delta n > 0.5$) and wide band gaps ($E_g > 3.5$ eV). Remarkably, benefiting from a maximal synergy of $[BS_3]^{3-}$ and $[SbS_3]^{3-}$ motifs achieved by an optimal assembly of 1D $[SbBS_4]_\infty$ chains, BaSbBS₄ was highlighted and then validated experimentally as the most promising IR birefringent crystal, unlocking a record high birefringence in the wide-band-gap range ($\Delta n = 0.95$ & 2.70 eV). This work not only discovers new high-performance birefringent crystals but also offers a universal avenue for precise and efficient evaluation of optical functional materials.

Introduction

Serving as critical components for linear and nonlinear optics, such as polarizers, wave plates and phase-matching elements, birefringent crystals have been utilized in a broad array of applications, including lithography, spectroscopy, optical polarization, phase compensators, remote sensing, polarization imaging, *etc.*[1–7] Exploring and optimizing the birefringent properties of crystals has attracted worldwide research interest. To date, there are only a few commercially available birefringent materials with restrictedly working wavelength ranging from the deep-UV to near-infrared region and limited birefringence values of 0.012–0.256, including MgF₂ (0.012 @ 400 nm),[8] α-BaB₂O₄ (0.116 @ 1064 nm),[9] TiO₂ (0.256 @ 546 nm),[10] CaCO₃ (0.172 @ 1064 nm),[11] YVO₄ (0.209 @ 1064 nm),[12] *etc.* However, in

the mid- and far-infrared regions, there is still a great shortage of available bulk birefringent materials. Hence, the exploration of high-performance mid- and far-infrared birefringent crystals is urgently needed. Chalcogenides are extensively regarded as a promising research system for exploring IR functional materials because of their wide IR transparency range, covering the important IR atmospheric windows, that is, 3–5 and 8–12 μm. Moreover, they exhibit rich structural diversities and enable various applications in nonlinear optics,[13–15] photocatalysis,[16] *etc.* Recently, scientists have discovered some interesting infrared birefringent chalcogenides, such as BaTiS₃ (0.76 & <1.0 eV),[17] Sr₉/₈TiS₃ (2.1 & <1.0 eV),[18] Cs₂S₆ (0.58 @ 1064 nm & 1.70 eV),[19] NaBaBS₃ (0.24 @ 1064 nm & 3.96 eV),[20] and ASb₅S₈ (A = K, Rb) (0.29 @ 1910 nm & 1.60 eV).[21] Unfortunately, their optical properties show an imbalance: the first three possess considerably large birefringence, but they can only be used in low-power optoelectronic devices[22] due to the non-negligible optical damage caused by the very small band gaps; while the others exhibit small birefringence, although they may have wider band gaps. Based on these facts, it is imperative to seek more balanced birefringent chalcogenides with both huge birefringence (>0.5) and relatively wide band gaps (>2.0 eV) to fill the gap in demand for high birefringence applied in high-power IR optical systems. However, achieving such optimal performance in a crystal is a serious challenge due to the naturally conflicting relationship between the two key metrics: E_g and Δn.[23,24]

aState Key Laboratory of Functional Crystals and Devices, Fujian Institute of Research on the Structure of Matter, Chinese Academy of Sciences, Fuzhou, 350002, P. R. China. E-mail: mjg@fjirsm.ac.cn; clhu@fjirsm.ac.cn

bUniversity of Chinese Academy of Sciences, Beijing 100049, P. R. China

† Electronic supplementary information (ESI) available: The details of deep learning model training, computational and experimental methods, ML-predicted or experimental band gaps and birefringence of screened compounds, crystal data, selected bond distances and bond valence, powder XRD, EDS, IR spectrum, TGA curve, birefringence measurement graphs, band structure, and density of states of BaSbBS₄. CCDC 2419693. For ESI and crystallographic data in CIF or other electronic format see DOI: https://doi.org/10.1039/d5sc01983d

Functional motifs (FMs) are microscopic modules responsible for materials' macro-performance and are of paramount importance. The common tetrahedra $[MS_4]$ and octahedra $[MS_6]$ in chalcogenides are less considered to be good Δn-active FMs because their polarizability anisotropy is very low (even zero) and depends highly on the distortions in specific structures. After careful evaluation based on quantum chemical computations, two kinds of anionic groups emerge as excellent IR Δn-active FMs. The stereochemically active lone pair (SCALP) groups, including $[AsS_3]^{3-}$, $[SbS_3]^{3-}$, $[SnS_3]^{4-}$ and $[BiS_3]^{3-}$, exhibit natural advantages in the birefringent material field because the SCALP electrons can induce the cations to undergo second-order Jahn–Teller (SOJT) distortion and endow the motifs with large polarizability anisotropies of 48.28, 36.87, 14.41 and 46.6 a.u., respectively. Meanwhile, they also possess wide HOMO–LUMO gaps ranging from 3.89 to 4.82 eV. Equally stunning is the π-delocalized planar $[BS_3]^{3-}$ FM, which fully integrates the merits of boron and sulfur elements, possessing a wider HOMO–LUMO gap of 5.37 eV and a nearly considerable polarizability anisotropy of 34.71 a.u. (Fig. 1). In consideration of the great structural diversity, the systems with SCALP-containing $[MS_3]$ or/and planar $[BS_3]^{3-}$ FMs would be a treasure for the exploration of balanced IR birefringent crystals.

With the rapid development of big data and artificial intelligence, an effective combination of high-throughput computational prediction fueled by machine learning and targeted experiments is becoming the ideal paradigm for materials discovery. It is target-driven and more efficient compared to the traditional 'trial-and-error' approach and has made exciting achievements in the materials design of thermoelectrics,[25] nonlinear optics[26,27] and energy systems.[28]

In this work, a target-driven closed-loop material discovery framework in coupling with functional motif and crystal structure screening, deep learning assisted high-throughput optical property computation and targeted experimental synthesis was developed. Using the framework, 150 compounds containing excellent Δn-active FMs, including $[BS_3]^{3-}$, $[AsS_3]^{3-}$, $[SbS_3]^{3-}$, $[SnS_3]^{4-}$, $[BiS_3]^{3-}$, etc., were screened from 12 748 inorganic chalcogenides in the Inorganic Crystal Structure

Database (ICSD) and a batch of superior IR birefringent crystals, including six with huge birefringence of $\Delta n > 1.0$ and three with both large birefringence ($\Delta n > 0.5$) and wide band gaps ($E_g > 3.5$ eV), were discovered. BaSbBS$_4$, in which the synergistic effect of $[BS_3]^{3-}$ and $[SbS_3]^{3-}$ is fully activated, was highlighted as the most promising IR birefringent crystal with optimally balanced performance of $\Delta n = 0.952$ and $E_g = 2.70$ eV. Furthermore, BaSbBS$_4$ was successfully synthesized, and its optical anisotropy was rigorously substantiated. Besides, a deep investigation of the origin of giant birefringence in BaSbBS$_4$ was conducted geometrically and electronically.

Methods

Our integrated workflow, namely a target-driven closed-loop material discovery framework, is displayed in Fig. 2, which shows an efficient discovery process of high-performance IR birefringent crystals. It consists of five important steps.

(1) Functional motif and crystal structure screening

Starting from quantum chemical calculations and selecting of birefringent functional motifs, with the aid of a fast structure screening technique, the crystal structures containing specific FMs with large polarizability anisotropy and wide HOMO–LUMO gaps are screened from the Inorganic Crystal Structure Database (ICSD), while eliminating the Δn-inactive cubic, disordered, nonstoichiometric structures and those containing metal–metal bonds. In this work, 150 compounds containing excellent Δn-active FMs, including $[BS_3]^{3-}$, $[AsS_3]^{3-}$, $[SbS_3]^{3-}$, $[SnS_3]^{4-}$, $[BiS_3]^{3-}$, etc., were screened out from 12 748 inorganic chalcogenides in the ICSD. It is noteworthy that uniaxial crystals are preferred owing to their ease of processing and manipulation, while biaxial crystals enable finer optical control and some with giant birefringence are also regarded as promising birefringent crystals, such as $Hg_4(Te_2O_5)(SO_4)$ (0.542 @ 546 nm),[29] $(C_5H_{6.16}N_2Cl_{0.84})(IO_2Cl_2)$ (0.67 @ 546 nm),[30] C_3H_8-$N_6I_6 \cdot 3H_2O$ (2.8 in the visible region).[1] So we take both uniaxial and biaxial crystals into consideration.
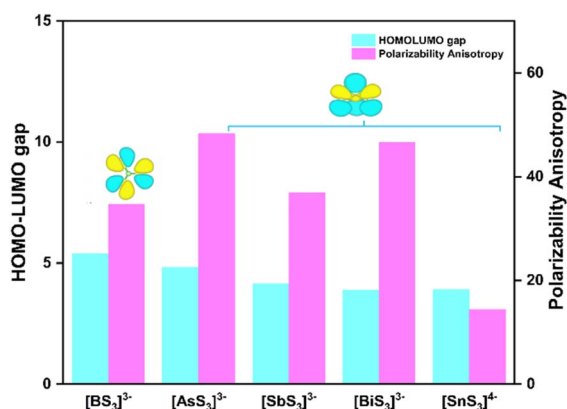

Fig. 1 HOMO–LUMO gaps and polarizability anisotropy of functional motifs.
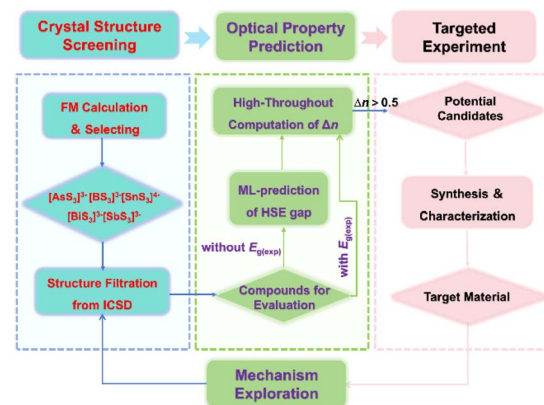

Fig. 2 A target-driven closed-loop material discovery framework for birefringent crystals.

(2) A deep learning model for precise band gap prediction

The optical property simulation of crystals is intrinsically dependent on precise band gap data. In consideration of limited experimental band gap data, serious band gap underestimation of DFT-PBE (Perdew–Burke–Ernzerhof), and non-negligible inefficiency of hybrid functional calculations, we developed a new deep learning model capable of predicting the band gaps of crystals at the HSE (Heyd–Scuseria–Ernzerhof) level (Fig. 3).

Our model is obtained by employing a transfer learning approach to fine-tune the parameters of a pretrained MatErials Graph Network (MEGNet) model (the architecture is shown in Table S1, ESI†)[31] based on a high-quality dataset comprising 10 481 materials with HSE-level computed band gaps from the Seoul National University Materials Data Center (SNUMAT) database.[32] It shows excellent prediction accuracy with a low mean absolute error (MAE) of 0.1205 eV and good fitting capability with a high coefficient of determination (R^2) of 0.9763 (close to 1) (Fig. S1a, ESI†). As an essential and powerful technique for efficiently and accurately predicting crystal bandgaps, the new deep learning model is integrated into our target-driven material discovery framework. The band gaps of the screened crystals are fast predicted by the model and show good agreement with the available experimental data (Table S2, ESI†).

(3) High-throughput computation of optical properties

The electronic structures (band structure, density of states, electron density, *etc.*) and linear optical properties (dielectric function, refractive index, birefringence, *etc.*) of all screened crystals are systematically calculated by employing DFT methods on a high-throughput computing platform created by us. It enables batch computation, automatic analysis and data extraction of electronic structures and optical properties of crystals, ensuring precise optical property assessments of a large number of crystals. Through this process, potentially excellent birefringent materials can be efficiently identified.

(4) Experimental synthesis and verification

The potential candidates are experimentally synthesized by employing the high-temperature solid-state method, and their optical properties are systematically characterized, thereby obtaining target materials and validating the prediction results.

Fig. 3 Illustration of the deep learning model for predicting the band gaps of crystals at the HSE level transferred from a pretrained MEGNet model.

(5) Mechanism investigation

The intrinsic origin underlying large birefringence and wide band gaps of crystals is deeply investigated from the perspectives of geometric and electronic structures. And using polarizability anisotropy-weighted electron density analysis (PAWED), the crystal orbitals that contribute to the birefringence of materials can be intuitively visualized, and the contribution percentage of each FM can be numerically identified. It provides a reliable theoretical basis and strategic support for the discovery and development of novel birefringent materials.

The details of model training, computational and experimental methods are provided in the ESI.†

Results and discussion

The birefringence and band gaps of the screened 150 compounds are listed in Table S2 (ESI)† and plotted in Fig. 4. The violin map (Fig. 4a) reveals that most of them exhibit band gaps within the range of 2.0–2.2 eV and birefringence values below 0.5. From Fig. 4b, it's found that there are as many as 32 compounds that have birefringence greater than 0.5 at 546 nm, accounting for 21% of the examined compounds, which indicates that our screening based on functional motif selection is very effective in discovering birefringent materials. The band gaps of the SCALP motif-containing compounds are mostly distributed in the range of 1.5–3.0 eV, and those of $[BS_3]^{3-}$ are in the 3.0–4.0 eV range. Among the 150 compounds, 10 are binary, 52 are ternary, 82 are quaternary, and 6 are quinary; and in the $\Delta n \geq 0.5$ category, there are 4 binary, 14 ternary, and 14 quaternary compounds (Fig. 4c).

Furthermore, there are up to six compounds with giant birefringence of $\Delta n > 1.0$ (Fig. 4b), which contain 4 thio-antimonites with mono-motif $[SbS_3]^{3-}$ (Sb_2S_3, $Sn_2Sb_2S_5$, $InSb_2$-S_4X (X = Cl, Br)),[33-35] 1 thiostannite with mono-motif $[SnS_3]^{3-}$ (SnS)[36] and 1 thioboroantimonite with multiple motifs $[SbS_3]^{3-}$ and $[BS_3]^{3-}$ ($PbSbBS_4$).[37] The four thioantimonites share similar geometric structures, featuring one-dimensional chains or two-dimensional layers. Sb_2S_3 shows well-aligned 1D neutral $[Sb_4S_6]_\infty$ slabs formed by two 1D chains of corner-sharing $[SbS_3]^{3-}$ groups and a central double chain of edge-sharing $[SbS_5]^{7-}$ groups (Fig. 5a). $Sn_2Sb_2S_5$ also features wide 1D $[Sn_4$-$Sb_4S_{10}]_\infty$ slabs constructed by central tetrameric chains of edge-shared $[SnS_5]^{8-}$ square-prisms grafted by four 1D chains of $[SbS_3]^{3-}$ units (Fig. 5b). Differently, $InSb_2S_4X$ (X = Cl, Br) exhibits a 2D layer composed of alternative $[Sb_4S_6]_\infty$ slabs as in Sb_2S_3 and $[In_2S_4X_2]_\infty^{4-}$ double chains of edge-sharing $[InS_4X_2]^{7-}$ octahedra (Fig. 5c). SnS adopts a corrugated layered structure in which the $[SnS_3]^{4-}$ pyramids are interconnected by corner-sharing μ^3-S atoms (Fig. 5d). The slightly staggered slabs in Sb_2S_3 and $Sn_2Sb_2S_5$ as well as the parallel-arranged layers in $InSb_2S_4X$ (X = Cl, Br) and SnS are very conducive to optical anisotropy and endow these biaxial crystals with giant birefringence values of 1.189, 1.058, 1.340, 1.253 and 1.312 at 546 nm, respectively. Evidently, the 1D and 2D chalcogenides composed of single SCALP anionic motifs have great potential as novel high-performance IR birefringent materials.
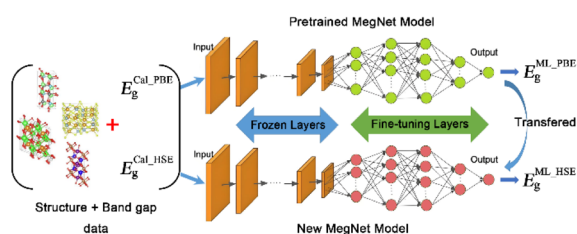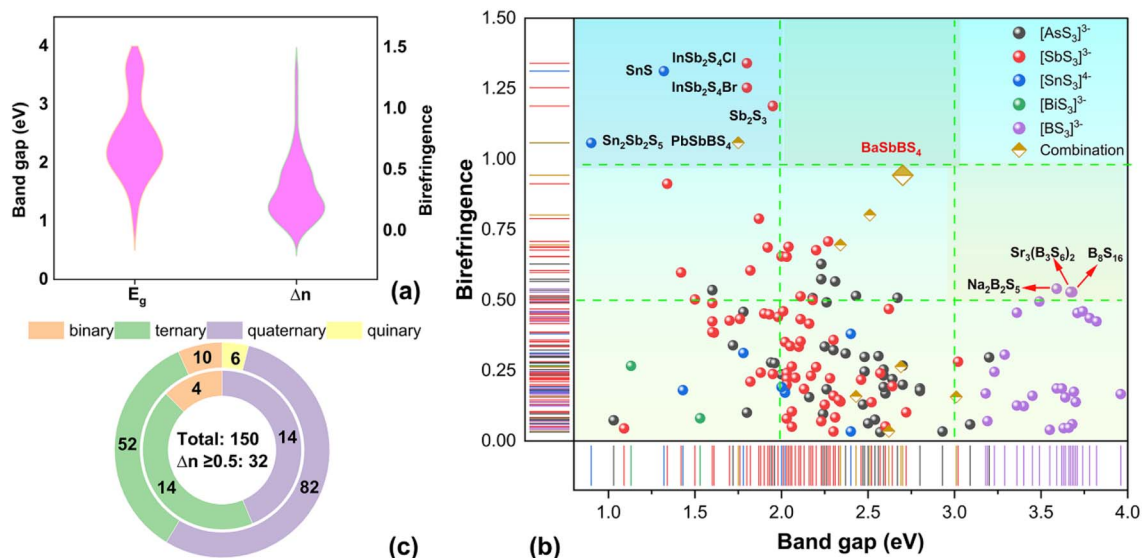
Fig. 4 (a) The violin map of band gap (eV) and Δn. (b) Birefringence-band gap map for all screened crystals (at 546 nm). (c) Distribution of stoichiometry of all screened crystals and highly birefringent ones among them.

Meanwhile, we also find that three thioborates ($Na_2B_2S_5$, $Sr_3(B_3S_6)_2$ and B_8S_{16})[38–40] not only possess large birefringence ($\Delta n > 0.5$), but also exhibit wide band gaps ($E_g > 3.5$ eV), achieving a simultaneous enhancement in optical anisotropy and band gap. This is not surprising, as the planar π-delocalized B–S units naturally reserve wide HOMO–LUMO gaps and large polarizability anisotropy. $Sr_3(B_3S_6)_2$ is a uniaxial crystal, whereas the other two are biaxial crystals. They all display 0D structures (Fig. 5e–g), the orderly arrangements of respective $[B_2S_5]^{2-}$, $[B_3S_6]^{3-}$ and $[B_8S_{16}]$ motifs lead to their significant birefringence (0.541, 0.529 and 0.529 @ 546 nm).

Remarkably, the combination of π-conjugated $[BS_3]^{3-}$ units and SCALP groups can achieve a superior birefringent performance, such as $PbSbBS_4$ and $BaSbBS_4$.[41] They are both biaxial crystals and feature perfect 1D infinite $[SbBS_4]_\infty^{2-}$ chains composed of corner-sharing $[BS_3]^{3-}$ and $[SbS_3]^{3-}$ (Fig. 5h and i). Their full cooperation results in a double increase in birefringence ($PbSbBS_4$: 1.05; $BaSbBS_4$: 0.943 at 546 nm) compared to the above thioborates. It is noted that $BaSbBS_4$ also retains a wide band gap of 2.70 eV. Clearly, $BaSbBS_4$ achieves an optimal balance between a wide band gap and giant birefringence by integrating the advantages of both $[BS_3]^{3-}$ and $[SbS_3]^{3-}$ motifs, making it a potential high-performance IR birefringent material.

Experimental synthesis

Based on the above screening results, we selected the compound $BaSbBS_4$ with the best overall performance for experimental validation. The single crystal of $BaSbBS_4$ was obtained through the high-temperature solid-state reactions in vacuum quartz tubes. Its structure was determined by single-crystal X-ray diffraction (XRD) studies (Fig. S2, ESI†). The details of crystal data and structure refinement parameters are shown in Table S3 (ESI).† The atomic coordinates and equivalent anisotropic displacement parameters are listed in Tables S4

(ESI),† and the selected bond distances, bond angles and bond valence sum (BVS) are presented in Table S5 (ESI).† Energy dispersive X-ray spectroscopy (EDS) analysis indicates that the single crystals of $BaSbBS_4$ are uniformly composed of Ba, Sb and S with a molar ratio of Ba/Sb/S of 1.00 : 1.05 : 3.91 (Fig. S3, ESI†), which is consistent with the chemical compositions determined from single crystal X-ray diffraction studies.

$BaSbBS_4$ crystallizes in the orthorhombic space group $Pnma$ with unit cell parameters of $a = 9.6601(12)$ Å, $b = 6.2154(7)$ Å, $c = 11.633(13)$ Å, $\alpha = 90°$, and $V = 698$ Å^3 (CCDC 2419693 contains the supplementary crystallographic data for this paper). In the structure, there is one Ba atom, one Sb atom, one B atom, and four S atoms in the asymmetric unit of $BaSbBS_4$. B^{3+} and Sb^{3+} form the triangular planar $[BS_3]^{3-}$ and trigonal pyramidal $[SbS_3]^{3-}$ units with the bond lengths ranging from 1.756(9) to 1.816(5) Å and 2.375(2) to 2.5199(14) Å, respectively. The S–B–S bond angles show minor deviations from the ideal trigonal planar value of 120°, and the angles of S–Sb–S are 97.68°, 97.68°, 76.65°. As shown in Fig. 5i, $[BS_3]^{3-}$ and $[SbS_3]^{3-}$ motifs are corner-sharing and interconnected alternately to form an infinite 1D chain of $[SbBS_4]_\infty^{2-}$. The Ba^{2+} ions act as spacers and counter cations to balance the charge. This crystal structure is consistent with the earlier reported one.[41]

The thermogravimetric analysis (TGA) curve (Fig. S4†) under a N_2 atmosphere revealed that $BaSbBS_4$ is stable up to 650 °C, which is lower than those of $Ca_2La(BS_3)(SiS_4)$ (880 °C)[42] and $Cs_2ZnAs_4S_8$ (700 °C),[43] but higher than those of $Sr(Ag_{1-x}Li_x)_2Se_2$ ($x = 0, 0.38$) (600 °C)[44] and $AZrPS_6$ (A = K, Rb, Cs) (470 °C).[45]

The infrared spectrum confirms the existence of element B in $BaSbBS_4$ (Fig. S5, ESI†). The prominent absorption band observed at approximately 850 cm^{-1}, along with the weaker absorption peak near 500 cm^{-1}, can be attributed to the asymmetrical B–S stretching E modes and the symmetrical A_1' modes of the $[BS_3]^{3-}$ unit, respectively. The splitting of the vibrational modes around 850 cm^{-1} is attributed to the
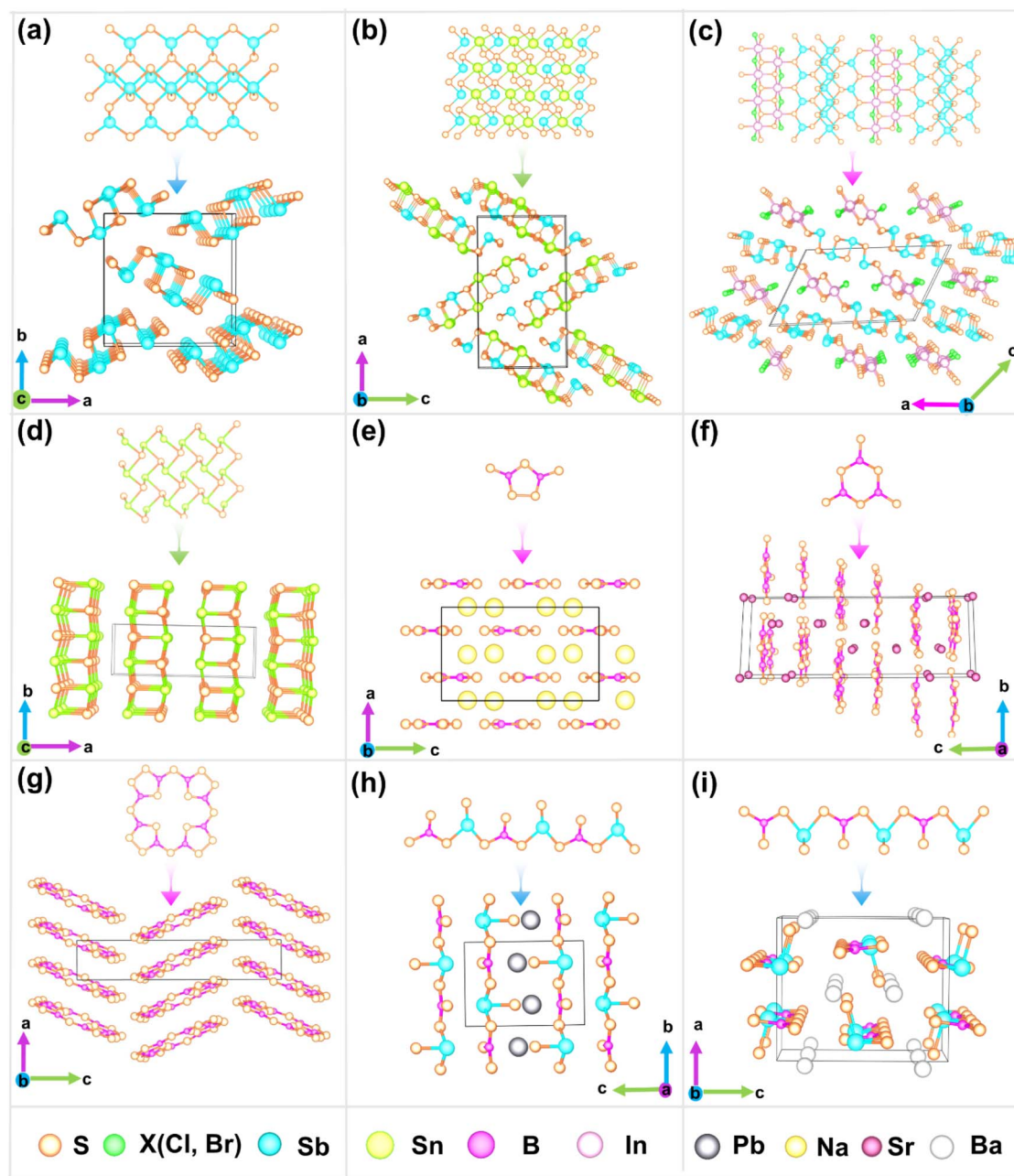
Fig. 5 Crystal structures of (a) Sb_2S_3, (b) $Sn_2Sb_2S_5$, (c) $InSb_2S_4X$ (X = Cl, Br), (d) SnS, (e) $Na_2B_2S_5$, (f) $Sr_3(B_3S_6)_2$, (g) B_8S_{16}, (h) $PbSbBS_4$, and (i) $BaSbBS_4$.

triangular distortion of the $[BS_3]^{3-}$ unit, resulting in a symmetry transition from D_{3h} to C_{2v}.[37] The IR spectrum shows the IR transparency range of $BaSbBS_4$ to be 2.5–11.8 μm, consistent with that observed in a previous study. Meanwhile, the reported UV-vis-NIR spectrum[41] revealed a band gap of 2.7 eV for $BaSbBS_4$, which is very close to the value we measured (2.64 eV, Fig. S6†).

Birefringent property evaluation

The birefringence of $BaSbBS_4$ was measured by polarization microscopy at 546 nm (Fig. 6a). Fig. S7a and b (ESI)† illustrate

the crystal before and after compensation with a tilting compensator under orthogonal polarizers. The birefringence is determined using the equation $R = \Delta n \times T$, where R is the optical path difference and T is the thickness of the single crystal, which were measured to be 8.6334 μm and 9.07 μm, respectively (Fig. S7c, ESI†). Hence, the experimental birefringence Δn_{exp} of $BaSbBS_4$ is 0.952 @ 546 nm, which is close to the calculated value of 0.943 @ 546 nm, surpassing most of the reported birefringent chalcogenides, such as $Cs_4Zn_5P_6S_{18}I$ (0.108 @ 546 nm),[46] $Ba_3(BS_3)(PS_4)$ (0.12 @ 546 nm),[47] Cs_2-$ZnSn_3S_8$ (0.120 @ 546 nm),[48] K_2BaGeS_5 (0.147 @ 546 nm),[49] α-
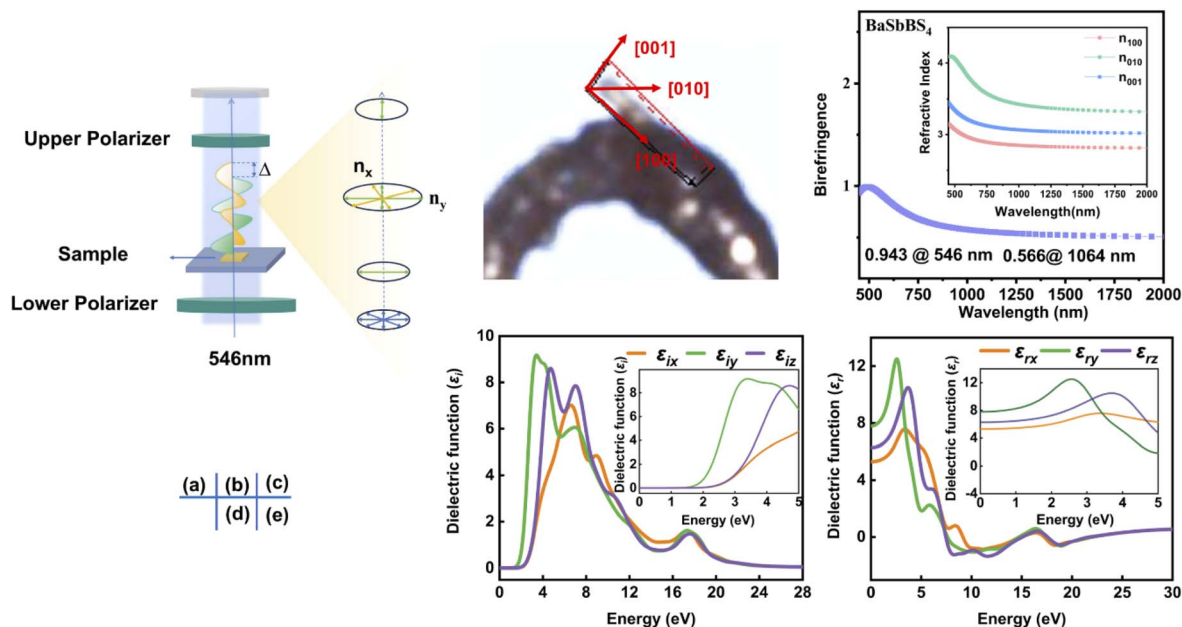
Fig. 6 (a) Schematic diagram for birefringence measurement. (b) Orientation of the BaSbBS$_4$ crystal determined by X-ray single-crystal diffraction. (c) Calculated refractive index and birefringence of BaSbBS$_4$. (d) Imaginary parts of the dielectric function. (e) Real parts of the dielectric function.

P$_4$S$_5$ (0.164 @ 546 nm),[15] LaBS$_3$ (0.17 @ 546 nm),[50] BaFS (0.238 @ 546 nm),[51] Cs$_3$In(In$_4$Se$_7$)(P$_2$Se$_6$) (0.28 @ 546 nm),[52] Hg$_2$P$_2$S$_6$ (0.65 @ 546 nm),[53] *etc.* Although some transition metal sulfides possess larger birefringence than BaSbBS$_4$, for example, Sr$_{9/8}$TiS$_3$ ($\Delta n = 2.1$)[18] and MoS$_2$ ($\Delta n = 1.5$),[54] they are only applicable in low-power optoelectronic devices due to the non-negligible optical damage caused by the very small band gaps (<1.0 eV for Sr$_{9/8}$TiS$_3$ and <2.0 eV for MoS$_2$). Also, MoS$_2$ gains optical applications more as thin films and nanomaterials rather than bulk crystalline materials. In contrast, the BaSbBS$_4$ crystal exhibits a huge birefringence and a wide band gap (0.952 & 2.70 eV) simultaneously, achieving an optimal balance between the two key property parameters. Remarkably, to the best of our knowledge, it approaches a record high birefringence in the wide-band-gap range ($E_g > 2.0$ eV) among the bulk chalcogenides. Hence, BaSbBS$_4$ is a promising IR birefringent crystal.

In the structure, the $[SbBS_4]_\infty^{2-}$ chain is perfectly parallel to the b axis, which leads to $n_{max} = n_{[010]}$, while the $[BS_3]^{3-}$ plane is perpendicular to the a axis, which leads to $n_{min} = n_{[100]}$ (Fig. 6b and c). So $\Delta n = n_{max} - n_{min} = n_{[010]} - n_{[100]} = \Delta n_{(001)}$, which is exactly the plane we determined (Fig. 6b). Besides, the calculated dielectric function curves also reveal the giant optical anisotropy in BaSbBS$_4$, whether the imaginary part (ε_i) or the real part (ε_r) (Fig. 6d and e). Interestingly, the absorption edge in the ε_{iy} curve is lower than those in ε_{iz} and ε_{ix} by 0.5–1.0 eV, and the corresponding first absorption peaks are located around 3.4, 4.7 and 6.6 eV, respectively, indicating that the stronger absorption occurs along the b axis in the low-frequency range. Meanwhile, the three real part curves of the dielectric function exhibit the trend of $\varepsilon_{ry} > \varepsilon_{rz} > \varepsilon_{rx}$ in the range of 0–3 eV, in good agreement with the refractive index curves.

Activation of the synergistic effect

Only a few chalcogenides combining triangular $[BS_3]^{3-}$ with SCALP-containing groups have been reported so far, and their chemical components and geometric structures have a great influence on the optical properties. We will take the Ba–B–Sb–S system as an example to systematically explore the component–structure–property relationship. Due to the wider HOMO–LUMO gap of $[BS_3]^{3-}$ than that of SCALP groups, a higher ratio of $[BS_3]^{3-}$ in such compounds may result in wider band gaps, which has been demonstrated in the band gap comparison of Ba$_6$(BS$_3$)$_3$(SbS$_3$) $[n(BS_3):n(SbS_3) = 3:1; E_g = 3.01$ eV][55] *versus* Ba$_3$(BS$_3$)(SbS$_3$) ($1:1$; 2.62 eV)[55] and BaSbBS$_4$ ($1:1$; 2.70 eV).

In contrast, the proportion of S^{2-} in the anionic frameworks can seriously influence their connectivity, arrangement and dimensionality, and thus affect the physical properties associated with the geometrically superposed feature. For example, in Ba$_6$(BS$_3$)$_3$(SbS$_3$) and Ba$_3$(BS$_3$)(SbS$_3$) with a S/(B + Sb) ratio of 3, both $[BS_3]^{3-}$ and $[SbS_3]^{3-}$ are isolated and alternately separated and the uneven arrangements lead to their smaller optical anisotropy ($\Delta n = 0.157$ and 0.035) compared to the single-motif compounds mentioned above. Obviously, such a combination is not always advantageous. However, when the S/(B + Sb) ratio decreases to 2 as in BaSbBS$_4$, the reduction of S^{2-} leads to the connection of $[BS_3]^{3-}$ with $[SbS_3]^{3-}$ by corner-sharing S atoms, forming 1D infinite$[SbBS_4]_\infty^{2-}$ chains. They are well aligned in the structure and result in a huge birefringence close to 1.0. Moreover, compared to Ba$_3$(BS$_3$)(SbS$_3$) (2.62 eV), the band gap of BaSbBS$_4$ is broadened to 2.70 eV due to the −B–S–Sb− connectivity (Fig. 7). It is conceivable that the hypothetical SbBS$_3$ with the smaller S/(B + Sb) ratio (1.5) could be further dimensionally enhanced and expected to be a promising birefringent crystal
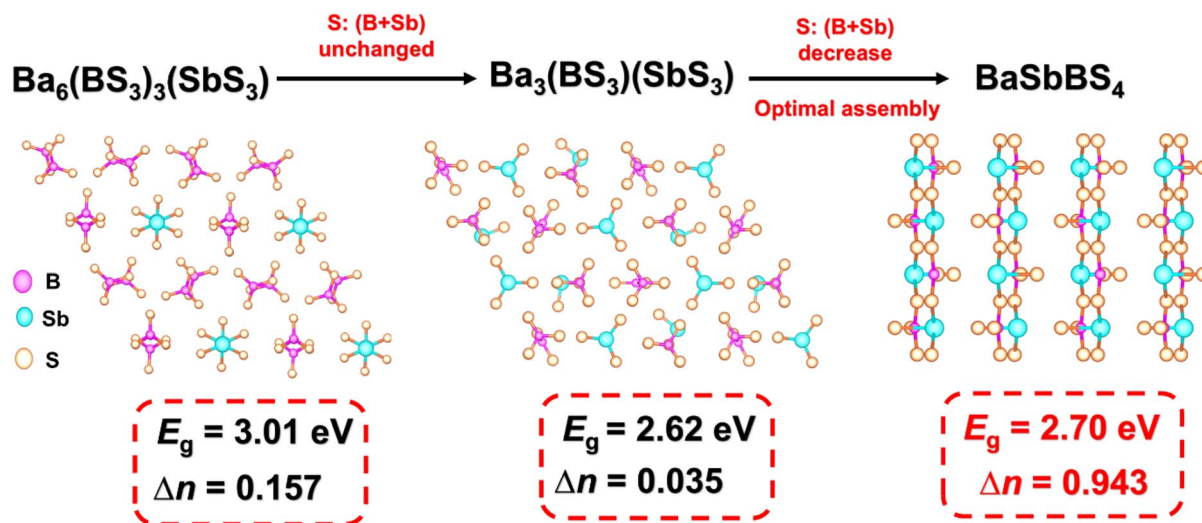
Fig. 7 Evolution from isolated $[BS_3]^{3-}$ and $[SbS_3]^{3-}$ motifs in $Ba_6(BS_3)_3(SbS_3)$ and $Ba_3(BS_3)(SbS_3)$ to the optimal assembled $[SbBS_4]_\infty^{2-}$ chains in $BaSbBS_4$. The synergistic effect of FMs is activated.

with great optical anisotropy, and the band gap is to be further widened due to more saturated S 3p non-bonding states resulting from a higher degree of connectivity between functional motifs.

Therefore, the reduction in S^{2-} proportion leads to an effective combination of $[BS_3]^{3-}$ with $[SbS_3]^{3-}$ groups in $BaSbBS_4$ and the synergistic effect of them is perfectly activated, causing a concurrent enhancement of birefringence and band gap.

Mechanism

Band structure calculation based on the GGA-PBE functional indicates that $BaSbBS_4$ is an indirect band gap compound and has a theoretical band gap of 2.26 eV (Fig. S8†), slightly smaller than the experimental value (2.70 eV).[41] The density of states (DOS) (Fig. S9†) illustrates that the upper part of the VB (−10–0 eV) is mainly consist of S 3p, B 2s2p and Sb 5s5p states, and the CB is composed of Ba 5d, B 2s2p, Sb 5p and S 3p empty orbitals, among which Sb 5s5p and B 2s2p are fully overlapped with the S 3p states, implying the strong covalent interactions of Sb–S and B–S bonds in the structure. Both the band structure and DOS are highly consistent with those reported in the previous study.[41] The highest VB is mostly contributed by the S 3p nonbonding states, and the lowest CB is from the unoccupied Sb 5p orbitals, hence the band gap of $BaSbBS_4$ is dominated by the $[SbS_3]^{3-}$ motifs.

As described above, $BaSbBS_4$ exhibits a balanced optical performance with a huge birefringence of ~1.0 and a wide band
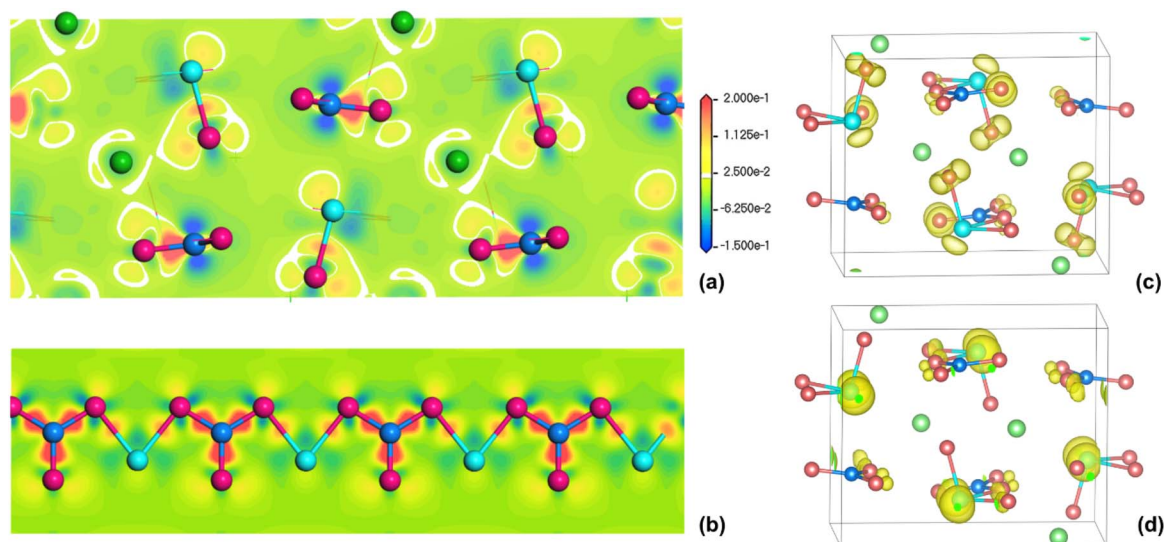

Fig. 8 The electron density difference (EDD) maps for Sb^{3+} $5s^2$ lone pairs (a) and the $[SbBS_4]_\infty^{2-}$ chain (b), and the polarizability anisotropy-weighted electron density (PAWED) plots for the VB (c) and CB (d).

gap of 2.70 eV concurrently, and shows superiority among infrared bulk birefringent materials. We will delve into the origin of large birefringence in $BaSbBS_4$ from the perspectives of both the geometric structure and electronic structure. First, the constituent motifs, planar π-delocalized $[BS_3]^{3-}$ and triangular pyramidal lone pair-containing $[SbS_3]^{3-}$, possess large polarizability anisotropy, and the strong stereochemical activity of the Sb^{3+} $5s^2$ lone pairs can be proved by the lobe-like isosurface on the Sb^{3+} ions from the electron density difference (EDD) map in Fig. 8a.

Second, $BaSbBS_4$ features a well-arranged 1D $[SbBS_4]_\infty^{2-}$ infinite chain, in which a maximized superposition of the polarizability anisotropy of $[BS_3]^{3-}$ and $[SbS_3]^{3-}$ motifs is achieved. It's because that for $[BS_3]^{3-}$, the maximal refractive index difference occurs between directions in and perpendicular to the molecular plane; while for SCALP-containing $[SbS_3]^{3-}$, that occurs between the normal plane of the LP and along the LP direction; and in the chain, the normal plane accommodating the SCALP of $[SbS_3]^{3-}$ and the $[BS_3]^{3-}$ plane are nearly coplanar. Moreover, the $[BS_3]^{3-}$ units in different chains along the b-axis are parallel to each other, extending in the bc-plane and perpendicular to the a-axis, causing an optimal superposition of optical anisotropy of all motifs in the structure, with the maximum refractive index occurring in the b-axis and the minimum in the a-axis. Third, compared to a 3D geometry, a low-dimensional (1D and 2D) covalent framework is more conducive to generating large optical anisotropy, because it can lead to a large difference in polarizable electron cloud density along different dielectric principal axes. As demonstrated in Fig. 8b, a huge contrast of electron density along and perpendicular to the $[SbBS_4]_\infty^{2-}$ chain is clearly observed.

To intuitively reveal the electronic orbitals that contribute to the large birefringence of $BaSbBS_4$, the polarizability anisotropy-weighted electron density (PAWED) analysis was performed. As shown in Fig. 8c and d, in the VB, the dominant contributor is the 3p nonbonding states of S atoms, especially the terminal S, mixed with some hybridized 5s5p lone-pairs of Sb atoms, and in the CB, the unoccupied Sb 5p and the π^*-antibonding orbitals of $[BS_3]^{3-}$ make a significant contribution to the large optical anisotropy of $BaSbBS_4$. Based on the PAWED data, the contribution percentages are quantified to be 46.07%, 50.47% and 3.46% for $[BS_3]^{3-}$, $[SbS_3]^{3-}$ and Ba^{2+}, respectively. Evidently, the huge birefringence of $BaSbBS_4$ originates from the synergistic effect of $[BS_3]^{3-}$ and $[SbS_3]^{3-}$ with considerable polarizability anisotropy.

Conclusions

In order to more efficiently explore excellent birefringent crystals from databases, a target-driven closed-loop material discovery framework, in coupling with functional motif and crystal structure screening, deep learning assisted high-throughput computation and targeted experimental synthesis was developed by us. Utilizing the framework, a batch of superior IR birefringent crystals containing Δn-active FMs of planar $[BS_3]^{3-}$ and/or SCALP groups ($[SbS_3]^{3-}$, $[SnS_3]^{4-}$, etc.) were identified from 12 748 inorganic chalcogenides in the

ICSD: six with huge birefringence ($\Delta n > 1.0$) and three with both large birefringence ($\Delta n > 0.5$) and wide band gaps ($E_g > 3.5$ eV). $BaSbBS_4$, which perfectly integrates the merits of $[BS_3]^{3-}$ and $[SbS_3]^{3-}$ FMs, was highlighted as the most promising IR birefringent crystal with balanced performance of $\Delta n = 0.952$ @ 546 nm and $E_g = 2.70$ eV, realizing a record high birefringence in the $E_g > 2.0$ eV range. Significantly, $BaSbBS_4$ was successfully synthesized and its optical anisotropy was rigorously substantiated. In addition, a complete and profound component–structure–property elucidation was performed, providing reliable strategic support for the development of a novel birefringent material. Our further efforts will be devoted to the large crystal growth and device preparation of the $BaSbBS_4$ crystal. This work not only discovers a record-high-performance IR birefringent material but also offers an efficient avenue for uncovering optical functional materials.

Data availability

The data that support the findings of this study are available in the ESI† of this article.

Author contributions

The manuscript was written through contributions of all authors. All authors have given approval to the final version of the manuscript.

Conflicts of interest

There are no conflicts to declare.

Acknowledgements

Notes and references

1 Y. Zhou, Z. Guo, H. Gu, Y. Li, Y. Song, S. Liu, M. Hong, S. Zhao and J. Luo, A solution-processable natural crystal with giant optical anisotropy for efficient manipulation of light polarization, *Nat. Photonics*, 2024, **18**, 922–927.

2 M. Mutailipu, K. R. Poeppelmeier and S. Pan, Borates: A Rich Source for Optical Materials, *Chem. Rev.*, 2021, **121**, 1130–1202.

3 A. Tudi, S. Han, Z. Yang and S. Pan, Potential optical functional crystals with large birefringence: recent advances and future prospects, *Coord. Chem. Rev.*, 2022, **459**, 214380.

4 L. E. MacKenzie and R. Pal, Circularly polarized lanthanide luminescence for advanced security inks, *Nat. Rev. Chem.*, 2021, **5**, 109–124.

5 N. A. Rubin, G. D'Aversa, P. Chevalier, Z. Shi, W. T. Chen and F. Capasso, Matrix Fourier optics enables a compact full-Stokes polarization camera, *Science*, 2019, **365**, 1839–1846.

6 X. Chen, W.-g. Lu, J. Tang, Y. Zhang, Y. Wang, G. D. Scholes and H. Zhong, Solution-processed inorganic perovskite crystals as achromatic quarter-wave plates, *Nat. Photonics*, 2021, **15**, 813–816.

7 L. H. Nicholls, F. J. Rodríguez-Fortuño, M. E. Nasir, R. M. Córdova-Castro, N. Olivier, G. A. Wurtz and A. V. Zayats, Ultrafast synthesis and switching of light polarization in nonlinear anisotropic metamaterials, *Nat. Photonics*, 2017, **11**, 628–633.

8 M. J. Dodge, Refractive properties of magnesium fluoride, *Appl. Opt.*, 1984, **23**, 1980–1985.

9 G. Guo, J. Xu, X. Chen, H. Zhong, S. Wang, K. Xu, P. Deng and F. Gan, Growth and spectrum of a novel birefringent α-BaB_2O_4 crystal, *J. Cryst. Growth*, 1998, **191**, 517–519.

10 W. M. Sinton, Birefringence of Rutile in the Infrared, *J. Opt. Soc. Am.*, 1963, **51**, 1309.

11 G. Ghosh, Dispersion-equation coefficients for the refractive index and birefringence of calcite and quartz crystals, *Opt. Commun.*, 1999, **163**, 95–102.

12 H. T. Luo, T. Tkaczyk, E. L. Dereniak, K. Oka and R. Sampson, High birefringence of the yttrium vanadate crystal in the middle wavelength infrared, *Opt. Lett.*, 2006, **31**, 616–618.

13 Y. Chu, H. Wang, Q. Chen, X. Su, Z. Chen, Z. Yang, J. Li and S. Pan, "Three-in-One": A New Hg-Based Selenide $Hg_7P_2Se_{12}$ Exhibiting Wide Infrared Transparency Range and Strong Nonlinear Optical Effect, *Adv. Funct. Mater.*, 2023, **34**, 2314933.

14 S. Yang, C. Lin, H. Fan, K. Chen, G. Zhang, N. Ye and M. Luo, Polar Phosphorus Chalcogenide Cage Molecules: Enhancement of Nonlinear Optical Properties in Adducts, *Angew. Chem., Int. Ed.*, 2023, **62**, e202218272.

15 X. Zhao, C. Lin, C. Wang, H. Tian, T. Yan, B. Li, N. Ye and M. Luo, Molecular Crystals Constructed by Polar Molecular Cages: A Promising System for Exploring High-performance Infrared Nonlinear Optical Crystals, *Angew. Chem., Int. Ed.*, 2024, **63**, e202319424.

16 S. Y. Tee, D. Ponsford, C. L. Lay, X. Wang, X. Wang, D. C. J. Neo, T. Wu, W. Thitsartarn, J. C. C. Yeo, G. Guan, T. C. Lee and M. Y. Han, Thermoelectric Silver-Based Chalcogenides, *Adv. Sci.*, 2022, **9**, e2204624.

17 S. Niu, G. Joe, H. Zhao, Y. Zhou, T. Orvis, H. Huyan, J. Salman, K. Mahalingam, B. Urwin, J. Wu, Y. Liu, T. E. Tiwald, S. B. Cronin, B. M. Howe, M. Mecklenburg, R. Haiges, D. J. Singh, H. Wang, M. A. Kats and J. Ravichandran, Giant optical anisotropy in a quasi-one-dimensional crystal, *Nat. Photonics*, 2018, **12**, 392–396.

18 H. Mei, G. Ren, B. Zhao, J. Salman, G. Y. Jung, H. Chen, S. Singh, A. S. Thind, J. Cavin, J. A. Hachtel, M. Chi, S. Niu, G. Joe, C. Wan, N. Settineri, S. J. Teat, B. C. Chakoumakos, J. Ravichandran, R. Mishra and M. A. Kats, Colossal Optical Anisotropy from Atomic-Scale Modulations, *Adv. Mater.*, 2023, **35**, e2303588.

19 G. Li, Z. Yang, X. Hou and S. Pan, Chain-like $[S_x]$ (x=2-6) Units Realizing Giant Birefringence with Transparency in the Near-Infrared for Optoelectronic Materials, *Angew. Chem., Int. Ed.*, 2023, **62**, e202303711.

20 Y. Yun, W. Xie, Y. Huang, Z. Yang, K. Wu, G. Li and S. Pan, $NaBaBS_3$: A Promising Infrared Functional Material with Large Birefringence Induced by π-Conjugated $[BS_3]$ Units, *Chem. Mat.*, 2022, **34**, 5215–5223.

21 W.-F. Chen, B.-W. Liu, S.-M. Pei, Q.-N. Yan, X.-M. Jiang and G.-C. Guo, ASb_5S_8 (A = K, Rb, and Cs): Thermal Switching of Infrared Nonlinear Optical Properties across the Crystal/Glass Transformation, *Chem. Mat.*, 2021, **33**, 3729–3735.

22 S. Manzeli, D. Ovchinnikov, D. Pasquier, O. V. Yazyev and A. Kis, 2D transition metal dichalcogenides, *Nat. Rev. Mater.*, 2017, **2**, 17033.

23 J. Lin, M.-H. Lee, Z.-P. Liu, C. Chen and C. J. Pickard, Mechanism for linear and nonlinear optical effects in β-BaB_2O_4 crystals, *Phys. Rev. B:Condens. Matter Mater. Phys.*, 1999, **60**, 13380.

24 F. Bassani, G. P. Parravicini, R. A. Ballinger and J. L. Birman, Electronic States and Optical Transitions in Solids, *Phys. Today*, 1976, **29**, 58–59.

25 Y. Gan, G. Wang, J. Zhou and Z. Sun, Prediction of thermoelectric performance for layered IV-V-VI semiconductors by high-throughput ab initio calculations and machine learning, *npj Comput. Mater.*, 2021, **7**, 176.

26 M. Wu, E. Tikhonov, A. Tudi, I. Kruglov, X. Hou, C. Xie, S. Pan and Z. Yang, Target-Driven Design of Deep-UV Nonlinear Optical Materials via Interpretable Machine Learning, *Adv. Mater.*, 2023, **35**, e2300848.

27 Q. Wu, L. Kang and Z. Lin, A Machine Learning Study on High Thermal Conductivity Assisted to Discover Chalcogenides with Balanced Infrared Nonlinear Optical Performance, *Adv. Mater.*, 2024, **36**, e2309675.

28 Z. Wang, H. Zhang and J. Li, Accelerated discovery of stable spinels in energy systems via machine learning, *Nano Energy*, 2021, **81**, 105665.

29 P. F. Li, C. L. Hu, Y. F. Li, J. G. Mao and F. Kong, $Hg_4(Te_2O_5)(SO_4)$: A Giant Birefringent Sulfate Crystal Triggered by a Highly Selective Cation, *J. Am. Chem. Soc.*, 2024, **146**, 7868–7874.

30 Q. Q. Chen, C. L. Hu, M. Z. Zhang and J. G. Mao, $(C_5H_{6.16}N_2Cl_{0.84})(IO_2Cl_2)$: a birefringent crystal featuring unprecedented $(IO_2Cl_2)^-$ anions and π-conjugated organic cations, *Chem. Sci.*, 2023, **14**, 14302–14307.

31 C. Chen, W. Ye, Y. Zuo, C. Zheng and S. P. Ong, Graph Networks as a Universal Machine Learning Framework for Molecules and Crystals, *Chem. Mat.*, 2019, **31**, 3564–3572.

32 S. Kim, M. Lee, C. Hong, Y. Yoon, H. An, D. Lee, W. Jeong, D. Yoo, Y. Kang, Y. Youn and S. Han, A band-gap database for semiconducting inorganic materials calculated with hybrid functional, *Sci. Data*, 2020, **7**, 387.

33 A. G. Vedeshwar, Optical Properties of Amorphous and Polycrystalline Stibnite(Sb_2S_3) Films, *J. Phys. III*, 1995, **5**, 1161–1172.

34 P. P. K. Smith and B. G. Hyde, The homologous series Sb_2S_3·nPbS: structures of diantimony dilead pentasulphide,

Pb$_2$Sb$_2$S$_5$, and the related phase diantimony ditin pentasulphide, Sn$_2$Sb$_2$S$_5$, *Acta Crystallogr., Sect. C:Cryst. Struct. Commun.*, 1983, **39**, 1498–1502.

35 W. Lei and H. Shiou-Jyh, A New Series of Chalcohalide Semiconductors with Composite CdBr$_2$/Sb$_2$Se$_3$ Lattices: Synthesis and Characterization of CdSb$_2$Se$_3$Br$_2$ and Indium Derivatives InSb$_2$S$_4$X (X =Cl and Br) and InM$_2$Se$_4$Br (M=Sb and Bi), *Chem. Mat.*, 2007, **19**, 6212–6221.

36 S. S. Hegde, P. Murahari, B. J. Fernandes, R. Venkatesh and K. Ramesh, Synthesis, thermal stability and structural transition of cubic SnS nanoparticles, *J. Alloys Compd.*, 2020, **820**, 153116.

37 L. Geng, W. D. Cheng, W. L. Zhang, Y. Y. Li, Z. Z. Luo, H. Zhang, C. S. Lin and Z. Z. He, Syntheses, crystal structures and characterizations of two new quaternary thioborates: PbMBS$_4$ (M = Sb, Bi), *Dalton Trans.*, 2011, **40**, 4474–4479.

38 C. Jansen, J. Kueper and B. Krebs, Na$_2$B$_2$S$_5$ and Li$_2$B$_2$S$_5$: two novel perthioborates with planar 1,2,4-trithia-3,5-diborolane rings, *Z. Anorg. Allg. Chem.*, 1995, **621**, 1322–1329.

39 A. Hammerschmidt, M. Doech, C. Puettmann and B. Krebs, Sr$_3$(BS$_3$)$_2$ und Sr$_3$(B$_3$S$_6$)$_2$: zwei neue nicht-oxidische chalkogenoborate mit trigonal-planar koordiniertem bor, *Z. Anorg. Allg. Chem.*, 2003, **629**, 551–555.

40 B. Krebs and H. U. Hürter, B$_8$S$_{16}$—An "Inorganic Porphine", *Angew. Chem., Int. Ed.*, 2003, **19**, 481–482.

41 L. Geng, W. D. Cheng, W. L. Zhang, C. S. Lin, H. Zhang, Y. Y. Li and Z. Z. He, BaM(BS$_3$)S (M = Sb, Bi): two new thioborate compounds with one-dimensional polymeric chain structure, *Inorg. Chem.*, 2010, **49**, 6609–6615.

42 Y. X. Han, C. L. Hu and J. G. Mao, Ca$_2$Ln(BS$_3$)(SiS$_4$) (Ln = La, Ce, and Gd): Mixed Metal Thioborate-Thiosilicates as Well-Performed Infrared Nonlinear Optical Materials, *Small*, 2024, **20**, e2305828.

43 C. Zhang, S.-H. Zhou, Y. Xiao, H. Lin and Y. Liu, Interesting dimensional transition through changing cations as the trigger in multinary thioarsenates displaying variable photocurrent response and optical anisotropy, *Inorg. Chem. Front.*, 2022, **9**, 5820–5827.

44 X. Zhou, B. Wilfong, X. Chen, C. Laing, I. R. Pandey, Y. P. Chen, Y. S. Chen, D. Y. Chung and M. G. Kanatzidis, Sr(Ag$_{1-x}$Li$_x$)$_2$Se$_2$ and [Sr$_3$Se$_2$][(Ag$_{1-x}$Li$_x$)$_2$Se$_2$] Tunable Direct Band Gap Semiconductors, *Angew. Chem., Int. Ed.*, 2023, **62**, e202301191.

45 S. Banerjee, J. M. Szarko, B. D. Yuhas, C. D. Malliakas, X. L. Chen and M. G. Kanatzidis, Room Temperature Light Emission from the Low-Dimensional Semiconductors AZrPS$_6$ (A = K, Rb, Cs), *J. Am. Chem. Soc.*, 2010, **132**, 5348–5350.

46 X. D. Chai, M. Z. Li, S. J. Lin, W. F. Chen, X. M. Jiang, B. W. Liu and G. C. Guo, Cs$_4$Zn$_5$P$_6$S$_{18}$I$_2$: The Largest Birefringence in Chalcohalide Achieved by Highly Polarizable Nonlinear Optical Functional Motifs, *Small*, 2023, **19**, e2303847.

47 J. Zhou, L. Wang, H. Wang, L. Luo, J. Li and F. Yu, Ba$_3$(BS$_3$)(PS$_4$): the first alkaline-earth metal thioborate-thiophosphate with strong optical anisotropy originating from planar [BS$_3$] units, *Dalton Trans.*, 2023, **52**, 16113–16117.

48 T. Tian, Z. Li, N. Wang, S. Zhao, J. Xu, Z. Lin and D. Mei, Cs$_2$ZnSn$_3$S$_8$: A Sulfide Compound Realizes a Large Birefringence by Modulating the Dimensional Structure, *Inorg. Chem.*, 2021, **60**, 9248–9253.

49 W. Xie, F. Li, J. Chen, Z. Yang, G. Li and S. Pan, Improved Birefringence Activated by Tetrahedra Decorated with a Single Linear Unit, *Angew. Chem., Int. Ed.*, 2023, **62**, e202307895.

50 Y.-X. Han, C.-L. Hu, Z. Fang, Q.-Q. Chen, B.-X. Li, Y. Lin and J.-G. Mao, LaBS$_3$ revisited: a promising mid-infrared nonlinear optical material, *J. Mater. Chem. C*, 2022, **10**, 12556–12559.

51 C. H. Xie, X. M. Jiang, B. W. Liu and G. C. Guo, BaFS: Birefringence Enhanced by the Transformation from Optical Isotropy to Anisotropy via Interlayer Anion Substitution, *Small*, 2025, **21**, e2409705.

52 Z. Qian, H. Wu, Z. Hu, J. Wang, Y. Wu and H. Yu, Cs$_3$In(In$_4$Se$_7$)(P$_2$Se$_6$): A Multi-Chromophore Chalcogenide with Excellent Nonlinear Optical Property Designed by Group Grafting, *Angew. Chem., Int. Ed.*, 2024, **63**, e202400892.

53 L.-J. Yao, C.-L. Hu, Z. Fang and J.-G. Mao, Hg$_2$P$_2$S$_6$: a layered mercury hexathiodiphosphate (IV) with large birefringence, *J. Solid State Chem.*, 2022, **315**, 123433.

54 G. A. Ermolaev, D. V. Grudinin, Y. V. Stebunov, K. V. Voronin, V. G. Kravets, J. Duan, A. B. Mazitov, G. I. Tselikov, A. Bylinkin, D. I. Yakubovsky, S. M. Novikov, D. G. Baranov, A. Y. Nikitin, I. A. Kruglov, T. Shegai, P. Alonso-Gonzalez, A. N. Grigorenko, A. V. Arsenin, K. S. Novoselov and V. S. Volkov, Giant optical anisotropy in transition metal dichalcogenides for next-generation photonics, *Nat. Commun.*, 2021, **12**, 854.

55 Y. Y. Li, B. X. Li, G. Zhang, L. J. Zhou, H. Lin, J. N. Shen, C. Y. Zhang, L. Chen and L. M. Wu, Syntheses, Characterization, and Optical Properties of Centrosymmetric Ba$_3$(BS3)$_{1.5}$(MS$_3$)$_{0.5}$ and Noncentrosymmetric Ba$_3$(BQ$_3$)(SbQ$_3$), *Inorg. Chem.*, 2015, **54**, 4761–4767.